The Astrophysical Journal Letters, 890:L18 (6pp), 2020 February 20 https://doi.org/10.3847/2041-8213/ab7237

Probing Cosmic-Ray Transport with Radio Synchrotron Harps in the Galactic Center

Timon Thomas[1], Christoph Pfrommer[1], and Torsten Enßlin[2]
[1] Leibniz-Institute for Astrophysics Potsdam (AIP), An der Sternwarte 16, D-14482 Potsdam, Germany; tthomas@aip.de
[2] Max Planck Institute for Astrophysics, Karl-Schwarzschild-Str. 1, D-85741 Garching, Germany
Received 2019 December 17; revised 2020 January 20; accepted 2020 January 30; published 2020 February 14

Abstract

Recent observations with the MeerKAT radio telescope reveal a unique population of faint nonthermal filaments pervading the central molecular zone, a region rich in molecular gas near the Galactic center. Some of those filaments are organized into groups of almost parallel filaments, seemingly sorted by their length, so that their morphology resembles a harp with radio-emitting "strings." We argue that the synchrotron-emitting GeV electrons of these radio harps have been consecutively injected by the same source (a massive star or pulsar) into spatially intermittent magnetic fiber bundles within a magnetic flux tube or via time-dependent injection events. After escaping from this source, the propagation of cosmic-ray (CR) electrons inside a flux tube is governed by the theory of CR transport. We propose to use observations of radio harp filaments to gain insight into the specifics of CR propagation along magnetic fields of which there are two principle modes: CRs could either stream with self-excited magnetohydrodynamic waves or diffuse along the magnetic field. To disentangle these possibilities, we conduct hydrodynamical simulations of either purely diffusing or streaming CR electrons and compare the resulting brightness distributions to the observed synchrotron profiles of the radio harps. We find compelling evidence that CR streaming is the dominant propagation mode for GeV CRs in one of the radio harps. Observations at higher angular resolution should detect more radio harps and may help to disentangle projection effects of the possibly three-dimensional flux-tube structure of the other radio harps.

Unified Astronomy Thesaurus concepts: Galactic center (565); Non-thermal radiation sources (1119); Cosmic rays (329); Computational methods (1965)

1. Introduction

Radio observations of the Galactic center region show many isolated, elongated filaments (Yusef-Zadeh et al. 1984, 2004; Lang et al. 1999; LaRosa et al. 2001; Nord et al. 2004). Recent high-resolution observations with the MeerKAT radio telescope found that the filaments trace bipolar bubbles that are rising from the central molecular zone (CMZ; Heywood et al. 2019). The filaments are characterized by a high aspect ratio, a filament-aligned magnetic field (Lang et al. 1999), strongly polarized emission (LaRosa et al. 2001), and a hard spectral index that steepens away from the geometric center of the filaments (Law et al. 2008). Hence, these nonthermal filaments (NTFs) are illuminated by synchrotron-emitting electrons.

Explanations for injecting relativistic electrons into NTFs include magnetic reconnection (Lesch & Reich 1992; Bicknell & Li 2001), acceleration in young stellar clusters (Yusef-Zadeh 2003), magnetized wakes of molecular clouds (Shore & LaRosa 1999; Dahlburg et al. 2002), pulsar wind nebula (Bykov et al. 2017; Barkov & Lyutikov 2019), stellar winds of massive stars (Rosner & Bodo 1996; Yusef-Zadeh & Wardle 2019), and even annihilation of light dark matter (Linden et al. 2011). Whether the origin of the parsec-sized straight NTFs is causally linked to the electron source that powers them is unclear.

To explain the brightness of NTFs, we need to take a closer look at cosmic-ray (CR) propagation. The Lorentz force ties CRs to any macroscopic magnetic field and causes the CRs to follow the field line motion. When magnetic fields are frozen into and move along with the fluid, CRs are bound to follow these fluid motions. This is called CR advection and shown in the left panel of Figure 1. We expect CR advection to be unimportant for NTFs as their straight morphology excludes large-scale gas motions perpendicular to the NTFs that change their appearance.

Of particular interest for NTFs is CR propagation along the mean magnetic field. It can be classified into two principle modes depending on the frequency of particle scatterings with magnetohydrodynamic (MHD) waves. (i) For frequent scatterings, the ensemble average of the particle distribution follows the motions of their nonrelativistic scattering centers while individual particles move with their relativistic velocities. This is the basis for describing CRs as a hydrodynamical fluid on scales larger than the effective mean-free path. (ii) For infrequent CR-wave scatterings, CRs move ballistically and individual particle trajectories obey a kinetic description. Malkov (2017) showed that CRs leave the ballistic regime after three characteristic scattering times and enter a diffusive, fluid-like behavior (middle panel of Figure 1).

For CRs with energies below $\sim$200 GeV, MHD waves are likely the dominant source of scattering (Yan & Lazarian 2011; Blasi et al. 2012). CRs can provide their own scattering centers by exciting Alfvén waves on scales comparable to their gyroradii through the gyroresonant instability (Kulsrud & Pearce 1969). These Alfvén waves interact with CRs so that the effective CR drift velocity approaches the Alfvén velocity, v_a, which is referred to as CR streaming.

CRs injected by a compact source excite Alfvén waves while leaving their acceleration site. These Alfvén waves are traveling in opposite directions along the magnetic field away from the source. Both leading fronts of Alfvén waves span an expanding region populated by CRs. Due to their confinement into this region, the CR population rarefies. Assuming perfect confinement, there is a sharp transition between locations that are occupied by or free of injected CRs (see the right panel of Figure 1).

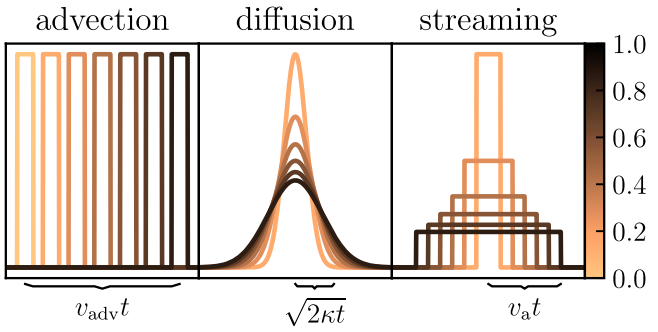

Figure 1. Archetypical transport modes of CR fluids. Left: CRs tied to frozen-in magnetic fields are advected with the bulk plasma velocity, $v_{\rm adv}$. Middle: when CRs are weakly scattered by Alfvén waves, they diffuse away from a given source (after an initial time) with an rms velocity of $\sqrt{2\kappa/t}$ (where t is the time and κ denotes the diffusion coefficient) along the magnetic field. Right: if CRs are effectively scattered, they stream with the Alfvén speed, $v_{\rm a}$, along the magnetic field.

This fundamental difference between CR streaming and diffusion allows us to differentiate between the two modes by studying the radio synchrotron brightness along NTFs: (i) the synchrotron emission from diffusing CR electrons smoothly fades away from a compact source while streaming CR electron populations show a central constant brightness level and a sharp transition to any background emission and (ii) as indicated in Figure 1, the rms distance of diffusing CR electrons increases as $\sqrt{2\kappa t}$, while in the CR streaming model, it increases linearly with time as $v_{\rm a}t$. If we were to observe equidistantly spaced snapshots of the two propagation modes, then the envelope of the snapshots should either show a bell shape (for CR diffusion), a triangle (for pure CR streaming), or an inverse bell shape (for CR streaming+diffusion).

In this Letter we are studying a particular class of NTFs that we call radio synchrotron harps and of which we show two examples in Figure 2. We will argue that those objects provide a rich avenue to study CR transport and propagation using radio observations.

2. Sources Powering NTFs

A massive star or pulsar moving through the CMZ with velocity $v_* \sim v_{\rm a}$ can intersect and inject CRs into a magnetic flux tube that has been stretched by the bipolar outflow from the CMZ (Heywood et al. 2019).

We conjecture that the regular arrangement of the harp "strings" in Figure 2 is created either by injecting CRs into spatially intermittent magnetic flux tubes or by a temporally intermittent injection process. Spatially intermittent magnetic fields are expected in magnetoturbulent environments such as the CMZ (Beresnyak & Lazarian 2015). Turbulent dynamo action can locally amplify the diffuse magnetic field from $\sim 10\,\mu$G to the observed 100–1000 μG in NTFs (Boldyrev & Yusef-Zadeh 2006). For temporally intermittent CR injection, CRs must be actively impeded from passing through the interface between the continuously accelerating source and the interstellar medium (ISM), possibly due to a temporarily missing magnetic connection through that interface, causing CR confinement.

In both cases, the different "string" lengths show a chronological sequence of CR injection events onto an NTF. After injection, the CRs propagate along the magnetic filament, which decreases their energy density and increases their spatial extent. Hence, NTFs with more recently injected CRs appear shorter and brighter while previously injected CRs form longer and fainter filaments. The resulting morphology is that of a filamentary isosceles triangle (or bell) with a bright apex and a fainter base- see Figure 2.

Wind termination shocks of massive stars—CR electrons generated at wind termination shocks or bow shocks of massive stars can illuminate NTFs (Rosner & Bodo 1996; Yusef-Zadeh & Wardle 2019). Massive stellar winds interact with their local ISM by building up an interaction layer between the wind interior and the ISM. This layer is confined by a bow shock that encompasses the shocked ISM and a wind termination shock. These shocked fluids are initially separated by a contact discontinuity, which becomes unstable to Rayleigh–Taylor instabilities that cause mixing of both fluids. At both shocks, electrons can be accelerated to relativistic energies via diffusive shock acceleration (e.g., del Valle & Pohl 2018). Some bow shocks are luminous enough for observable synchrotron emission (Benaglia et al. 2010, for a runaway-O-star bow shock). The stand-off radius R between star and bow shock is given by the pressure balance between stellar wind and ISM:

$$R = \left(\frac{\dot{M} v_\infty}{4\pi(\rho_{\rm ISM} v_\star^2 + P_{\rm ISM} + B^2/8\pi)}\right)^{1/2} \sim 0.05\ {\rm pc}, \quad (1)$$

where $\dot{M} \sim (10^{-8}$–$10^{-5}) M_\odot\ {\rm yr}^{-1}$ is the mass-loss rate, $v_\infty \sim (1000$–$2500)\,{\rm km\ s}^{-1}$ is the terminal wind velocity, $v_\star \sim$ few $\times\ 10\,{\rm km\ s}^{-1}$ is the relative velocity of the star, $\rho_{\rm ISM}$ and $P_{\rm ISM}$ are the ambient ISM density and pressure, and B is the ISM magnetic field strength. At a distance of 8.2 kpc to the CMZ, this corresponds to an angular scale of 8″, close to the observational resolution of 6″ (Heywood et al. 2019). We assume that the NTFs are embedded in the warm CMZ phase with gas temperature $T = 10^4\,{\rm K}$ and number density $n = 100\,{\rm cm}^{-3}$. This implies magnetically dominating NTFs with $B \sim 200\,\mu$G and a plasma beta $\beta = P_{\rm ISM}/(B^2/8\pi) = 2c_s/v_{\rm a} \sim 0.1$, which explains the straight NTF morphology that is not affected by turbulent gas motions. The stellar wind kinetic luminosity is

$$L_{\rm wind} = \frac{1}{2}\dot{M} v_\infty^2 \sim 1 \times 10^{35}\ {\rm erg\ s}^{-1} \quad (2)$$

so that the wind termination shock is

$$\frac{L_{\rm wind}}{L_{\rm bow}} = \frac{\dot{M} v_\infty^2}{\rho_{\rm ISM} v_\star^3 2\pi R^2} \sim 10^2 \quad (3)$$

times more powerful than the bow shock, implying that the termination shock dominates the CR acceleration. Assuming that all kinetic wind energy is dissipated at the wind termination shock and an electron acceleration efficiency of 0.1%, the total CR electron luminosity is

$$L_e = 1 \times 10^{-3}\, L_{\rm wind} \sim 1 \times 10^{32}\ {\rm erg\ s}^{-1}. \quad (4)$$

Magnetized winds of rotating stars result in perpendicular termination shocks that can accelerate electrons (Xu et al. 2019) but not protons (Caprioli & Spitkovsky 2014).

While moving through the ISM, the stellar wind bubble piles up a magnetic draping layer at the contact discontinuity. Accelerated electrons diffuse onto these field lines and escape from their acceleration site. Subsequently, they move away

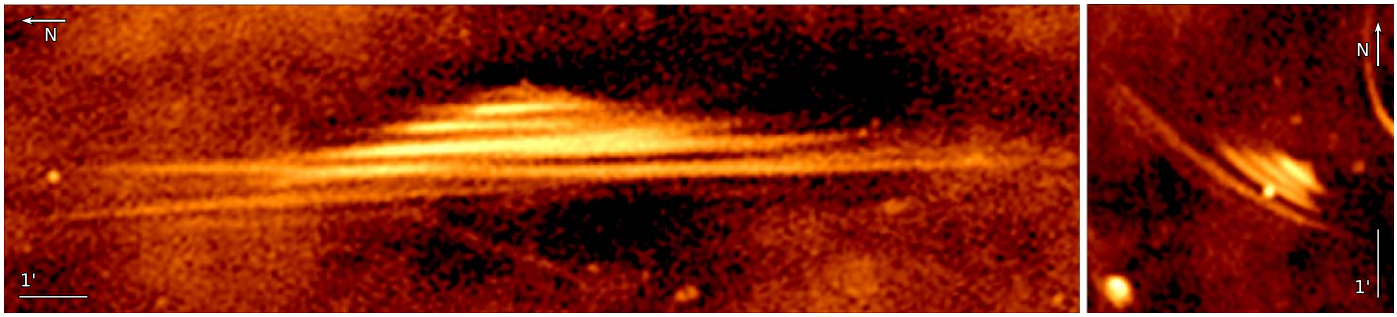

Figure 2. Two radio harps in the MeerKAT observation of the CMZ (Heywood et al. 2019). Left: the NTF G359.85+0.39 was discovered by LaRosa et al. (2001), also named N10 in Law et al. (2008). Right: G359.47+0.12 was first imaged by Heywood et al. (2019). Their names correspond to their position in Galactic coordinates.

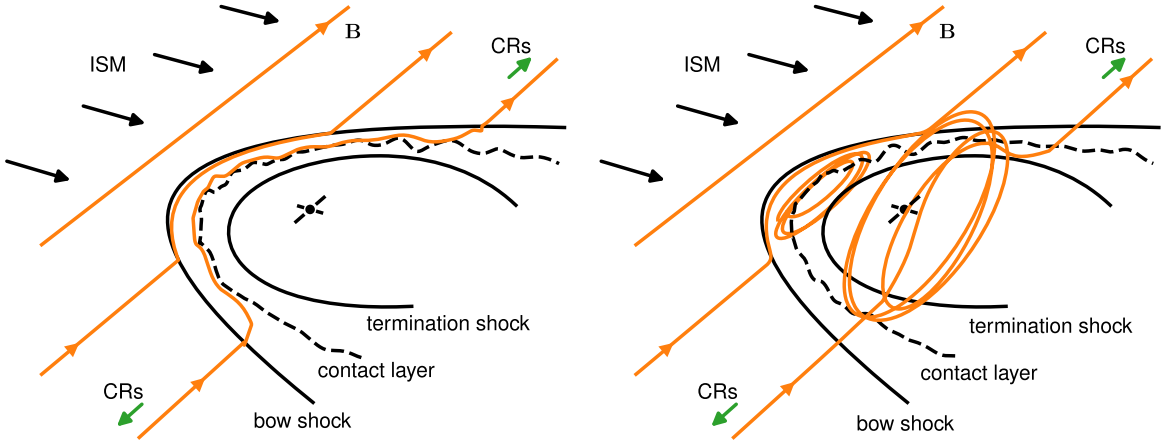

Figure 3. Sketches of possible scenarios that can inject CRs into NTFs. Left: a massive star located in the center drives a stellar wind that terminates at a shock. This shock accelerates CRs, which diffuse onto draped ISM magnetic fields, which experienced mixing with the shocked wind via Rayleigh–Taylor instabilities and escape into the ISM. Right: a pulsar drives the wind by accelerating electron–positron pairs toward the wind termination shock. Piled-up field lines behind the wind termination shock can reconnect with the ISM magnetic field, allowing CRs to escape.

from the star, emit synchrotron radiation in the strongly magnetized ISM flux tubes, and illuminate the NTFs (see the left panel of Figure 3).

Pulsar winds—Another possible source of CR electrons for NTFs are pulsar wind nebulae (PWN; Barkov & Lyutikov 2019). PWNs are fueled by a central pulsar with a spin-down luminosity $\dot{E} \sim 5 \times 10^{37}\,\mathrm{erg\,s^{-1}}$. The wind is launched at the light cylinder of the pulsar's magnetosphere, where electron–positron pairs leave the magnetosphere and are accelerated by the strong electromagnetic fields. Further acceleration can take place in reconnection layers of the striped pulsar wind. Similar to a stellar wind, the pulsar wind is separated from the ISM by a layer consisting of the wind termination shock, a contact discontinuity, and a possible bow shock. An ISM magnetic field that is draped around the pulsar wind can reconnect at the contact discontinuity with the magnetic field originating from the wind interior (Barkov & Lyutikov 2019; Barkov et al. 2019). This allows relativistic particles to escape from the PWN into the ISM; see the right panel of Figure 3. The stand-off distance of the pulsar wind is

$$R = \left(\frac{\dot{E}}{4\pi c(\rho_{\rm ISM} v_\star^2 + P_{\rm ISM} + B^2/8\pi)}\right)^{1/2} \sim 0.05\ \mathrm{pc}. \quad (5)$$

Not all electrons leave the PWN so that the luminosity of NTF-injected electron–positron pairs is

$$L_e = 2.5 \times 10^{-4}\frac{\dot{E}}{\sigma} \sim 1 \times 10^{32}\,\mathrm{erg\,s^{-1}}, \quad (6)$$

where $\sigma \sim 100$ is the pulsar wind magnetization.

If this pulsar-scenario holds true, then the observed number of $>10^2$ NTFs (Heywood et al. 2019) indicates a pulsar population in the CMZ. If every NTF hosts a pulsar and the produced CR electrons inverse-Compton scatter and radiate in γ-rays, then this can explain the Galactic center excess seen with the *Fermi* γ-ray telescope (Bartels et al. 2016; Lee et al. 2016; Fermi-LAT Collaboration 2017; Barkov & Lyutikov 2019).

Radio emission from NTFs—Both scenarios are comparable in terms of their energy budget and size of the acceleration site. Thus, the energy injected into a flux tube,

$$E_{\rm CR} = f_{\rm esc}\frac{R}{v_\star}L_e \sim 5 \times 10^{42}\,\mathrm{erg}, \quad (7)$$

is the same for both sources. Here, $f_{\rm esc} \sim 0.3$–1 is the time fraction during which CRs near the wind termination shock are injected into a flux tube. Furthermore, assuming that the injected electrons/pairs have a Lorentz factor $\gamma \sim 10^3$, they

emit synchrotron radiation at

$$\nu = \frac{3eB\gamma^2}{2\pi m_e c} \sim 1.5\ \mathrm{GHz} \tag{8}$$

with a total luminosity of

$$L_{\mathrm{syn}} = E_{\mathrm{CR}} \frac{\sigma_{\mathrm{T}} B^2 \gamma}{6\pi m_e c} \sim 2 \times 10^{29}\ \mathrm{erg\ s^{-1}}, \tag{9}$$

which corresponds to a spectral flux of

$$F_{\mathrm{syn}} = \frac{L_{\mathrm{syn}}}{2\pi d^2 \nu} \sim 2\ \mathrm{mJy} \tag{10}$$

at a distance of $d = 8.2$ kpc. Within the uncertainties, this matches the radio harp flux. The associated synchrotron cooling time of $\sim 10^6$ yr is much longer than the CR propagation time of $\sim$60 kyr so that we do not expect synchrotron fading (see Section 3).

3. Hydrodynamic Flux Tube Model for Radio Harps

Already the detection of radio harps is a strong argument in favor of CR propagation with v_{a}: CRs leaving the source have individual trajectories that are preferentially aligned with the magnetic flux tube. As NTFs lay mostly perpendicular to the Galactic plane, the synchrotron radiation should be beamed away from the Galactic plane and undetectable for us. Thus, to explain the NTF detection, some mechanism is needed that effectively scatters CRs such that their beamed radiation is observable with radio telescopes. A likely possibility is pitch-angle scattering by gyroresonant Alfvén waves. CRs moving along a flux tube can excite these Alfvén waves via the gyroresonant instability, which leads to CR streaming close to the Alfvén speed, v_{a} (see Section 1).

We model CR electron propagation inside NTFs with the following numerical setup: we assume self-similar evolution of the individual filaments in a harp and that the observation samples the NTF evolution at different times. Within a propagation model, this allows us to conduct a single simulation for all filaments. Filaments of different lengths correspond to different simulation times: longer filaments correspond to later times with a broadened CR distribution.

We assume an Alfvén speed of $v_{\mathrm{a}} = 40\ \mathrm{km\ s^{-1}}$ and use ISM parameters as detailed in Section 2. The simulation domain is aligned with the magnetic flux tube, which is assumed to be straight and to have a constant cross section πR^2 during the simulation. The CR electrons are initialized by injecting $E_{\mathrm{CR}} = 5 \times 10^{42}$ erg into a Gaussian with width 0.05 pc to model CR injection at the bow shock of a massive star or pulsar.

1. The diffusion model assumes that the CRs diffuse along the magnetic flux tubes with a constant coefficient $\kappa = 3 \times 10^{25}\ \mathrm{cm^2\ s^{-1}}$, which was chosen to match NTF sizes with a diffusion length scale $l = \sqrt{2\kappa t}$ and $t = 30$ kyr.[3] We include Alfvén wave cooling of CRs (see Pfrommer et al. 2017).
2. The streaming+diffusion model uses the more accurate CR transport description of Thomas & Pfrommer (2019), which evolves the CR energy and momentum density. Additionally, the energy contained in gyroresonant Alfvén waves is evolved and coupled to CRs using quasi-linear theory of CR transport. We only consider nonlinear Landau damping of Alfvén waves (see Thomas & Pfrommer 2019). The initial CR energy flux is chosen so that CRs stream with v_{a}.

[3] In the diffusion model, only the combination κt is constrained by the diffusion length; for simplicity, we use the timescale of the streaming +diffusion model.

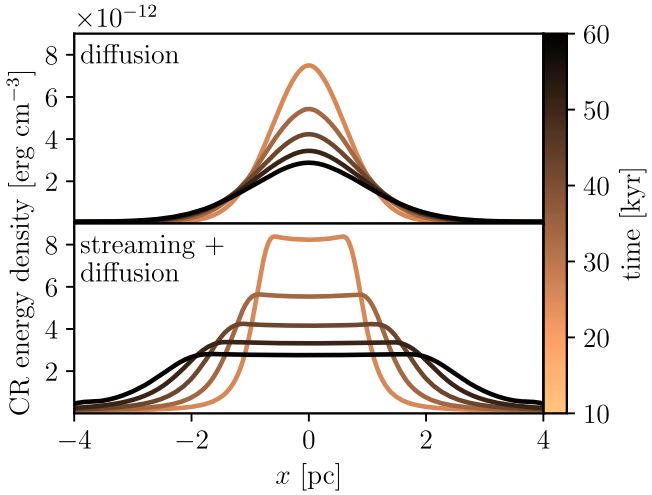

Figure 4. Evolution of the energy densities of CR electrons for the two propagation models over the course of 60 kyr.

The streaming+diffusion model includes details of the microphysical CR–Alfvén-wave interactions that are absent in the pure diffusion model. In comparison to the diffusion model (where κ = const.) the diffusion coefficient in the streaming +diffusion model is calculated based on the local strength of Alfvén waves. We solve the equations of Thomas & Pfrommer (2019) using a finite volume method (T. Thomas et al. 2020, in preparation) in the moving mesh code AREPO (Springel 2010) for both models (in the diffusion model we set κ = const). We use a one-dimensional grid with 4096 cells, a grid spacing of $\Delta x = 4 \times 10^{-3}$ pc, and outflowing boundary conditions. A reduced speed of light $\tilde{c} = 1000\ \mathrm{km\ s^{-1}}$ is used and we confirmed that the presented results are robust for changes of $\tilde{c}$.

We present the CR electron energy density evolution in Figure 4. The result for the diffusion model resembles the typical evolution of a diffusion process: the initial Gaussian approximately maintains its shape while increasing its physical extent. The deviations from a pure diffusion profile are caused by CR energy losses due to Alfvén wave cooling.

Including CR–Alfvén-wave interactions allows CRs to enter the CR streaming regime. Therein the two Gaussian wings are traveling at speeds of $\sim \pm\, v_{\mathrm{a}}$ in opposite directions. In between the two wings the CRs are rarefied causing the development of an almost constant-energy–density plateau. At later times, the CRs are unable to maintain a high energy level of Alfvén waves. Consequently, CRs get less frequently scattered and enter the diffusive CR transport regime.

4. Comparison to Observations

We extract radio brightness profiles of the MeerKAT filaments (Heywood et al. 2019) by taking cuts along individual filaments of the harp G359.47+0.12, shown in Figure 2 on the right. We use one segment for the three brightest filaments, respectively, and four segments for the faintest filament to trace its curvature. In Figure 5, we compare

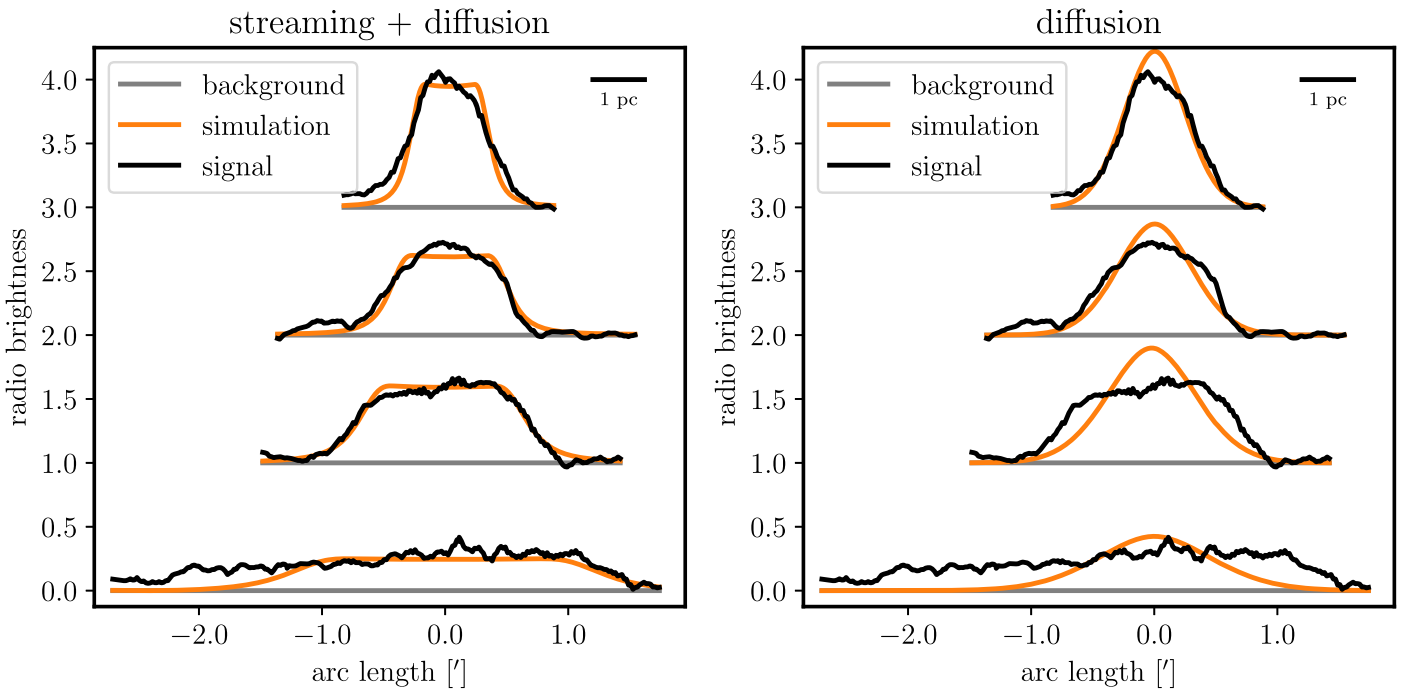

Figure 5. Comparison between the observed radio emission from the radio harp G359.47+0.12 (extracted from Heywood et al. 2019) and the simulated profiles. The simulated profiles are displayed at times 16, 26, 37, and 72 kyr (top to bottom) after CR injection. The filaments each have an offset of 1 in the *y*-direction. We convert physical distances in the simulation to angular sizes assuming a distance of 8.2 kpc to the CMZ. The streaming+diffusion model matches the MeerKAT radio data significantly better than the diffusion model.

this to our simulations by scaling the simulated CR energy density with a constant factor to match the observed radio flux. This factor is chosen so that the brightness in the first filament approximately agrees with the scaled simulated profiles. To match the brightness of the third and fourth filaments in the streaming+diffusion model, we had to increase the scaling by 25% and 40%, respectively. For the diffusion model, we need to increase these factors by 50%. The displayed background noise level is calculated by averaging the diffuse background excluding resolved and bright sources.

Only the streaming+diffusion model agrees with the observed profiles while the diffusion model is unable to reproduce the late-time central flat emission because the diffusion profile maintains its central maximum, causing there to be excess emission, and underestimates the emission at larger distances. The gradients of the diffusion profile progressively flatten, whereas the observations maintain sharp edges. Contrarily, the flat plateaus and sharp late-time gradients are well explained in the streaming+diffusion model. Therein, the plateau naturally corresponds to the rarefying CR energy density while the expanding CR fronts match the steep transition of the radio emission.

There are no primary beam corrections applied to the four pointings that make up the MeerKAT mosaic (Heywood et al. 2019). While this precludes accurate photometry of the large-scale emission, the small-scale radio harp profiles should mostly be unaffected. We note that the image of G359.47+0.12 shows a circularly shaped area with reduced flux levels of filaments and background emission, which is centered just outside the image in the lower right part of Figure 2. This reduced flux might be an artifact of the lacking primary beam corrections during imaging (Heywood et al. 2019) and could explain the asymmetric shape of the older synchrotron filaments in Figure 5. If correct, the agreement of the streaming+diffusion model with the observation may improve even more after primary beam corrections and the diffusion model will become worse, strengthening our finding.

We attempted to apply the same analysis to the harp G359.85+0.39. However, its filaments appear to be overlapping in projection. Whether the overlap is caused by the projection of individual spatially separated or of braided flux tubes that divert away from the central bright emission is not obvious. This ambiguity precludes a simple emission modeling of the complex flux-tube structure. However, the morphological similarity of both harps, which exhibit the shape of an inverted bell curve, strongly suggests that CR streaming is responsible for the emission structure in both cases.

We predict a massive star or pulsar at the tip of each radio harp and encourage observers to search for them.

5. Conclusions

Here, we presented a model that explains the morphological appearance of the new phenomenon of radio harps observed within the bipolar outflows by MeerKAT. A careful modeling of two competing CR transport schemes (pure CR diffusion and a combination of CR streaming and diffusion in the self-confinement picture) demonstrates that only the CR streaming model is able to match the detailed brightness distributions of the individual NTFs of the harp G359.47+0.12. The intermittency of the harp emission either reveals details of the magnetic field structure or about the magnetic reconnection processes at the interface of the shocked stellar (or pulsar) wind with the surrounding interstellar magnetic field. We hope that future high-resolution observations enable us to disentangle the possibly three-dimensional structure of the other harp G359.85 +0.39 and to detect more examples of this phenomenon. This will consolidate our conclusions that CR streaming is the relevant propagation mode for GeV CRs.

We thank Heywood et al. (2019) for providing the MeerKAT data and our referee for an insightful report. T.T. and C.P. acknowledge support by the European Research Council under ERC-CoG grant CRAGSMAN-646955. This research was supported in part by the National Science Foundation under grant No. NSF PHY-1748958.

ORCID iDs

Christoph Pfrommer https://orcid.org/0000-0002-7275-3998

References

Barkov, M. V., & Lyutikov, M. 2019, MNRAS, 489, L28
Barkov, M. V., Lyutikov, M., & Khangulyan, D. 2019, MNRAS, 484, 4760
Bartels, R., Krishnamurthy, S., & Weniger, C. 2016, PhRvL, 116, 051102
Benaglia, P., Romero, G. E., Martí, J., Peri, C. S., & Araudo, A. T. 2010, A&A, 517, L10
Beresnyak, A., & Lazarian, A. 2015, in Magnetic Fields in Diffuse Media, Astrophysics and Space Science Library, Vol. 407, ed. A. Lazarian, E. M. de Gouveia Dal Pino, & C. Melioli (Berlin: Springer), 163
Bicknell, G. V., & Li, J. 2001, ApJL, 548, L69
Blasi, P., Amato, E., & Serpico, P. D. 2012, PhRvL, 109, 061101
Boldyrev, S., & Yusef-Zadeh, F. 2006, ApJL, 637, L101
Bykov, A. M., Amato, E., Petrov, A. E., Krassilchtchikov, A. M., & Levenfish, K. P. 2017, SSRv, 207, 235
Caprioli, D., & Spitkovsky, A. 2014, ApJ, 783, 91
Dahlburg, R. B., Einaudi, G., LaRosa, T. N., & Shore, S. N. 2002, ApJ, 568, 220
del Valle, M. V., & Pohl, M. 2018, ApJ, 864, 19
Fermi-LAT Collaboration 2017, arXiv:1705.00009
Heywood, I., Camilo, F., Cotton, W. D., et al. 2019, Natur, 573, 235
Kulsrud, R., & Pearce, W. P. 1969, ApJ, 156, 445
Lang, C. C., Anantharamaiah, K. R., Kassim, N. E., & Lazio, T. J. W. 1999, ApJL, 521, L41
LaRosa, T. N., Lazio, T. J. W., & Kassim, N. E. 2001, ApJ, 563, 163
Law, C. J., Yusef-Zadeh, F., & Cotton, W. D. 2008, ApJS, 177, 515
Lee, S. K., Lisanti, M., Safdi, B. R., Slatyer, T. R., & Xue, W. 2016, PhRvL, 116, 051103
Lesch, H., & Reich, W. 1992, A&A, 264, 493
Linden, T., Hooper, D., & Yusef-Zadeh, F. 2011, ApJ, 741, 95
Malkov, M. A. 2017, PhRvD, 95, 023007
Nord, M. E., Lazio, T. J. W., Kassim, N. E., et al. 2004, AJ, 128, 1646
Pfrommer, C., Pakmor, R., Schaal, K., Simpson, C. M., & Springel, V. 2017, MNRAS, 465, 4500
Rosner, R., & Bodo, G. 1996, ApJL, 470, L49
Shore, S. N., & LaRosa, T. N. 1999, ApJ, 521, 587
Springel, V. 2010, MNRAS, 401, 791
Thomas, T., & Pfrommer, C. 2019, MNRAS, 485, 2977
Xu, R., Spitkovsky, A., & Caprioli, D. 2019, arXiv:1908.07890
Yan, H., & Lazarian, A. 2011, ApJ, 731, 35
Yusef-Zadeh, F. 2003, ApJ, 598, 325
Yusef-Zadeh, F., Hewitt, J. W., & Cotton, W. 2004, ApJS, 155, 421
Yusef-Zadeh, F., Morris, M., & Chance, D. 1984, Natur, 310, 557
Yusef-Zadeh, F., & Wardle, M. 2019, MNRAS, 490, L1